Modeling Cavitation over Axisymmetric Bodies: VOF Technique versus Boundary Element Method

H. Moin[1], I. Rashidi[2], Mohammad P. Fard[3], Mahmoud P. Fard[4] and E. Roohi[5]

[1,2,3,4]*Department of Mechanical Engineering, Ferdowsi University of Mashhad*
Mashhad, Iran

[5]*Department of Aerospace Engineering, Sharif University of Technology*
Tehran, Iran

Email: mpfard@um.ac.ir

ABSTRACT

A computational study of super- and partial-cavitation over axisymmetric bodies is presented using two numerical methods. The first method is based on the VOF technique where the transient Navier-Stokes equations are solved along with an equation to track the cavity interface. The second method is that of the steady boundary element method (BEM) which is a model based on the potential flow theory. The supercavitation results of the two methods for disk and cone cavitators are compared with each other and with those of the available experiments and analytical relations. Two different geometries for a cone with various cone angles are considered. Also, the results of comparison between the two methods for partial cavitation over a sphere, a blunt cylinder, and a cylinder with a spherical head are presented.

1. INTRODUCTION

The cavitation phenomenon is known as liquid vaporization that occurs whenever the liquid pressure falls bellow its vapor pressure. This phenomenon is categorized by a nondimensional parameter called cavitation number:

$$\sigma = (P_\infty - P_v)/(\tfrac{1}{2}\rho V_\infty^2) \quad (1)$$

where P_v is the vapor pressure, ρ the liquid density, and P_∞, V_∞ are the main flow pressure and velocity, respectively.

The cavitation regimes are classified to incipient-, shear-, cloud-, partial- and super-cavitation depending on the cavitation number [1]. The cavitation occurs around axisymmetric bodies at points where the local pressure drops to the environment vapor pressure. Any sudden change in the body shape may cause a pressure rise or fall and, therefore, may be an inception point for cavitation. Although super-cavitation decreases drag forces extensively, but when maneuvering of the vehicle is necessary, partial cavitation is more preferable [2]. Also, partial cavities are widely used in ventilated systems [2, 3].

During the last decades, numerous studies have been performed in cavitation using various methods [1]. Cavitation models based on the Navier-Stokes equations emerged in early 1990's. These models are divided into two main categories: interface tracking method and homogeneous equilibrium flow [4]. In interface tracking method, a constant pressure (vapor pressure) is assumed for the cavity region and a wake model is used to predict the shape of the cavity in adaptive grids. In the second category, used in this study, a single-fluid modeling approach is employed for both phases. Various models in this category differ in the calculation of the variable density field. In the Volume-of-Fluid (VOF) model, an advection equation for liquid volume fraction is solved and density is obtained based on the volume fraction of the two phases. Yuan et al. [5] suggested a cavitation model based on Rayleigh relation. Singhal et al. [6], Merkle et al. [7] and Kunz et al. [8] have used different mass transfer models based on semi-analytical equations. A well-known method to solve the advection of a free-surface such as a cavity interface is VOF technique. Frobenius and Schilling [9] and Wiesche [10] used this technique to simulate cavitation over hydrofoils and pump impellers. A review of the reported literature reveals that the VOF method can accurately capture cavity shape and characteristics. In this study, a modified VOF technique based on Youngs' PLIC algorithm [11] is combined with a mass transfer model of Kunz et al. [8] to simulate cavitation.

Cavitation can also be modeled by potential flow theory using the boundary element method (BEM). Early works on this method for partial cavitation were performed by Varghese, et al. [2], but using BEM to solve potential flow about arbitrary bodies were developed after Hess and Smith's paper [12]. Several researchers [13-16] used nonlinear BEM to model cavitation for hydrofoils. They distributed sources and normal dipoles along the solid body-cavity interface. The unknown values of these sources and dipoles were determined by imposing the dynamic condition on an assumed cavity boundary. The kinematic boundary condition was then used to update the cavity shape. Beginning in 1994, two numerical hydrodynamic models were developed for axisymmetric supercavitating high-speed bodies: a slender-body theory model (Varghese, et al, [17]) and a BEM method (Kirschner, et al, [18]; Uhlman, et al, [19]). The results of both the slender-body theory and the BEM method have been shown to compare well with other numerical and experimental results. These models can predict the shape and length of cavity, accurately. The BEM method was employed to examine supercavitating flows past disk, cone and sigma-shaped cavitators where good agreements with experimental and analytical results have been reported [20].

In this paper, super- and partial-cavitation for water flows over axisymmetric bodies is studied using both of the above methods. For the VOF method, a modified Young's PLIC algorithm is used to advect the interface between the two phases. For the BEM method, sources and normal dipoles are distributed along the body-cavity surface. The unknown values of the source and dipole strengths are then obtained using the mixed Fredholm integral equation that results from the application of Green's third identity.

2. GOVERNING EQUATIONS

The two methods of VOF and BEM are briefly discussed in this section. The VOF method is based on the solution of the full Navier-Stokes equations along with an equation for the advection of cavity interface. The BEM method, however, is based on the concept of potential flow theory.

2.1 VOF method

In this method, the advection of the cavity interface is simulated based on the Volume-of-Fluid (VOF) technique along with a cavitation model for mass transfer between the two phases. The governing equations for the 2D/axisymmetic incompressible fluid flow are

$$\vec{\nabla}.\vec{V} = 0 \tag{2}$$

$$\frac{\partial \vec{V}}{\partial t} + \vec{\nabla}.(\vec{V}\vec{V}) = -\frac{1}{\rho}\vec{\nabla}P + \frac{1}{\rho}\vec{\nabla}.\vec{\tau} + \frac{1}{\rho}\vec{F}_b + \vec{g} \tag{3}$$

where $\vec{V}$ is the velocity vector, P indicates the pressure, F_b is the body force acting on the fluid, $\vec{g}$ is the acceleration due to the gravity and τ represents the viscous stress tensor. The phase change boundary is defined by a scalar field f whose value is equal to zero in the vapor phase and one in the liquid. When a cell is partially filled with the liquid, f has a value between zero and one. The discontinuity in f is propagating through the computational domain based on [1]:

$$\frac{df}{dt} = \frac{\partial f}{\partial t} + \vec{V}.\vec{\nabla}f = S \tag{4}$$

where S is the cavitation mass transfer sink term. This equation with different mass transfer models can be used to simulate many physical phenomena such as cavitation, vaporization, and condensation.

Several cavitation mass transfer models can be used to replace S in Eq. 4. Among the more recommended models we have the Rayleigh equation and semi-analytical schemes [1]. Many semi-analytical schemes are based on the modified Rayleigh theory or a mass-momentum interaction model around the cavity interface [21]. In current study, the semi-analytical model of Kunz is used to treat S in Eq. 4:

$$\frac{\partial f}{\partial t} + \vec{V}.\vec{\nabla}f = \frac{C_{dest}\rho_l Min(P_l - P_v, 0)f}{(\tfrac{1}{2}\rho_l V_\infty^2)\rho_v t_\infty} + \frac{C_{prod}(1-f)f^2}{\rho_l t_\infty} \tag{5}$$

where $C_{dest} = 9\times10^5$ and $C_{prod} = 3\times10^4$ are numerical-experimental weighting coefficients [1]. The flow characteristic time, t_∞, is defined as the ratio of the maximum solid-body diameter to the main flow velocity. The second term in the right hand side of Eq. 5 is for the condensation that occurs near the cavity closure region. This phenomenon causes small vapor structures to detach from the end of the cavity. The Kunz model assumes a moderate rate of constant condensation; therefore, it reconstructs the cavity region more accurately than the other models [1, 21].

The Hirt-Nichols [22] and Young PLIC [11] methods are widely used for the advection of the volume fraction in Eq. 4. Although the Hirt-Nichols has been used in most cavity simulations, in this study a more accurate method of Young is employed. To begin the advection using Eq. 4, an intermediate value of is introduced as:

$$\tilde{f} = f^n - \delta t \vec{\nabla}.(\vec{V} f^n) \tag{6}$$

and "divergence correction" completes the scheme:

$$f^{n+1} = \tilde{f} + \delta t (\vec{\nabla}.\vec{V}) f^n + \delta t (S^n) \tag{7}$$

This scheme initiates the distribution of f for velocity and pressure calculations in each time step. Two-step time projection method is employed for the solution of momentum equations. First, an intermediate velocity is calculated based on the terms related to advection, viscosity and body forces:

$$\frac{\tilde{\vec{V}} - \vec{V}^n}{\delta t} = -\vec{\nabla}(\vec{V}\vec{V})^n + \frac{1}{\rho^n}\vec{\nabla}.\vec{\tau} + \vec{g}^n + \frac{1}{\rho^n}\vec{F}_b^n \tag{8}$$

Continuum Surface Force (CSF) method [23] is used to treat the surface tension in interfacial cells as a body force. Pressure field is obtained by Poisson equation as:

$$\vec{\nabla}.(\frac{1}{\rho}\vec{\nabla}P^{n+1}) = \frac{\vec{\nabla}.\tilde{\vec{V}}}{\delta t} \tag{9}$$

Finally, the pressure field is used to compute the new time velocities:

$$\frac{\vec{V}^{n+1} - \tilde{\vec{V}}}{\delta t} = -\frac{1}{\rho}\vec{\nabla}P^{n+1} \tag{10}$$

An Incomplete Cholesky Conjugate Gradient Decomposition (ICCG) solver is employed for solving Eq. 9. Having calculated the new time level pressures, the velocities are updated using Eq. 10.

2.2 Boundary element method

The potential flow model presented here is based on Green's third identity formulation. Applying this formulation to the axisymmetric disturbance velocity potential, φ, results in [2]:

$$2\pi\varphi(r,x) = \iint_S \left\{ \frac{\partial\varphi}{\partial n} G(x,r;\xi,R) - \varphi(r,x)\frac{\partial G(x,r;\xi,R)}{\partial n} \right\} R\, d\varphi\, ds \tag{11}$$

where n is the normal vector directed outward from the body surface and the cavity interface, s is the arclength along a meridian, and x and r are the components of the axisymmetric coordinate system. $G(x,r;\xi,R)$ is the potential function related to the fluid sources distributed along a ring of radius R located on the axis at $x = \xi$ (see Fig 1). The potential function is defined as:

$$\begin{aligned} G(x,r;\xi,R) &= R\mathrm{J}_1^0(A,B) \\ &= \int_{-\pi}^{+\pi} \frac{\rho d\varphi}{\sqrt{(x-\xi)^2 + r^2 + R^2 - 2rR\cos(\varphi)}} \end{aligned} \tag{12}$$

where $\mathrm{A} = \mathrm{r}^2 + \mathrm{R}^2 + (x-\xi)^2$ and $\mathrm{B} = 2\mathrm{rR}$. And also

$$\begin{aligned} \mathrm{J}_1^0(A,B) &= \frac{4}{\sqrt{A+B}}\mathrm{K}(\mathrm{k}) \\ \mathrm{K}(\mathrm{k}) &= \int_0^{\pi/2} \frac{d\varphi}{\sqrt{1-\mathrm{k}^2\sin^2(\varphi)}} \\ k^2 &= \frac{2B}{A+B} \end{aligned} \tag{13}$$

Eq. 12 states that the potential flow on any surface can be shown by means of the ring distribution of sources and dipoles. For this purpose, the rings of the sources is distributed on the cavity surface, and also the rings of the dipoles is distributed on the body and the cavity surface (Fig.2).

The boundary conditions are kinematic condition on the body surface, and both the kinematic and dynamic conditions on the cavity interface. These conditions are mathematically formulated as:

$$\frac{\partial\phi}{\partial n} = 0 \quad \text{on } S_b \cup S_c \tag{14}$$

$$\frac{\partial\phi}{\partial s} = \sqrt{1+\sigma} \quad \text{on } S_c \tag{15}$$

where S_b and S_c are the areas of the body surface and the cavity interface, respectively.

3. RESULTS AND DISCUSSION

The supercavity formation behind several 2D/ axisymmetric cavitators, and partial cavitation around more-complex geometries is studied using both the VOF and BEM methods. The fluid considered for simulation is water with thermodynamic properties at 25ºC. The mesh size for the VOF simulations was set based on a previous study on cavitation [1] with one cell per one millimeter.

3.1 Supercavitation

The first case considered is that of the supercavitation behind a disk cavitator for which the experimental measurements and analytical relations are available in the literature. Reichardt analytical relation for supercavitation behind a simple cavitator is given by [24]:

$$\frac{l_{cavity,\max}}{d_{cavity,\max}} = \frac{\sigma + 0.008}{\sigma(1.7\sigma + 0.066)} \tag{16}$$

$$\frac{d_{cavity\,\max}}{D_{cavitator}} = \left[\frac{C_D}{\sigma(1-0.132\sigma^{0.5})} \right]^{0.5} \qquad (17)$$

where $l_{cavity,max}$ and $d_{cavity,max}$ are the maximum length and diameter of the cavity, respectively, and $D_{cavitator}$ represents the maximum diameter of cavitator.

Figure 3 compares the results of the two methods (VOF and BEM) with those of the available experiments [25] and the Reichardt relation (Eq. 16) for a disk cavitator. As observed from the figure, the results of both methods agree well with those of the experiments [25] and theory for high cavitation numbers ($\sigma > 0.15$). For lower cavitation numbers, while the VOF predictions are in good agreement with that of the Reichardt relation, the BEM method slightly overpredicts the experimental measurements.

Palset and Schaffer proposed an analytical relation for the drag coefficient of a simple cavitator for cavitation numbers less than 1.5 which reads [25]:

$$C_D = C_{D_0}(1+\sigma+0.028\,\sigma^2) \qquad (18)$$

where C_{D_0} is equal to 0.8053 for a disk cavitator. The comparison between the results of the two methods, the experiments [25], and the Palset-Schaffer relation (Eq. 18) for the drag coefficient is displayed in Fig. 4. The VOF method predictions are seen to be in better agreement with measurements compared to those of the BEM method.

Figure 5 shows the dimensionless cavity length vs. cavitation number for a cone cavitator with an angle of 90º. Both methods predict well the results of the experiments and analytical relations for high cavitation numbers ($\sigma > 0.15$). Small discrepancies, however, are seen between the results for lower cavitaion numbers. The drag coefficient against cavitation number for this case is displayed in Fig. 6. Both methods accurately predict the analytical results of the Palset-Schaffer relation (Eq. 18 with C_{D_0} equal to 0.518). The figure also displays the drag coefficient for a cone cavitator with an angle of 30º. The analytical relation which is used for this cone angle is again Eq. 18 but with a value of 0.205 for C_{D_0} [25]. As seen from the figure, the results from both VOF and BEM methods are in good agreement with each other. The analytical relation, however, slightly overpredicts the numerical results as the cavitation number is decreased.

The VOF method also provides the distribution of the velocity and pressure coefficient as displayed in Fig. 7 for a cone cavitator under consideration with an angle of 90º. Close inspection of the velocity profile inside the cavity region (left image of Fig. 7) reveals the existence of a reentrant jet at the cavity closure region. Three-dimensional views of the cavity region from the two methods are shown in Fig. 7 as well. The VOF predicted shape of the cavity shows two extra features. The cavity diameter is increased near the closure region due to the existence of the reentrant jet. The cavity interface is also seen to have ripples caused by the shear stress effects between the two phases of liquid and vapor. The BEM method does not predict the reentrant jet phenomenon; the method needs a more sophisticated model for treating the closure region.

The supercavitation behind a sphere is studied next. The variation of dimensionless cavity length against cavitation number for a sphere is shown in Fig. 8. The two model results compare well with each other. Since no analytical relation has been proposed for the cavitation formation behind a sphere, the Reichardt analytical relation for a disk cavitator (Eq. 16) is also shown in the figure to show the difference between the two geometries. It can be seen that the cavity length behind a disk cavitator is longer than that of a sphere.

The VOF results for pressure coefficient and velocity distribution for a sphere are presented in Fig. 9. The figure also shows three-dimensional views of the cavity from both methods. The reentrant jet is clearly visible from the VOF simulation. While the results of the two methods for the length of the cavity compares well with each other, a large discrepancy is seen between the two results for the cavity diameter. This discrepancy may be explained as follows. In the BEM model, the cavitation starts at a larger angle from the stagnation point in front of the sphere. This method, however, does not account for the existence of the re-entrant jet. As no experiments were available for this case, the actual physical phenomenon remains to be investigated.

3.2 Partial cavitation

Partial cavitation for a blunt cylinder and a cylinder with a spherical head is considered in this study. Figure 10 shows the pressure coefficient (C_P) versus nondimensional length for a blunt cylinder for a cavitation number of 0.3. As observed, both methods of VOF and BEM accurately predict the experimentally measured cavity length. Discrepancies between the results are seen at the end of the cavity region where the cavity closes on the cylinder body ($3.5 < L/D < 4$ in Fig. 10). In this region, the C_P variation from the BEM method shows an overshoot which may be attributed to the simple model used in this method for the cavity termination on the solid body. The VOF method, however, well predicts the experimental results for both the cavity length and its closure behavior. Figure 11 shows 3D views from both methods along with details of pressure and velocity distribution from the VOF

technique. The shape of the cavity in the closure region is significantly affected by the reentrant jet visible from the VOF results.

The variation of the pressure coefficient along the cavity for a cylinder with a spherical head for a cavitation number of 0.2 is displayed in Fig. 12. Similar to the previous case, the VOF method results is an accurate prediction of the C_P for the entire cylinder and even near the closure region. The BEM predictions, however, show inaccuracies at the closure region. The method for the rest of the cylinder well predicts the measurements. Figure 13 presents the results of the VOF method for the velocity distribution and pressure coefficient along with 3D views of the cavity region from both the VOF and BEM methods. The results of the two methods again differ in the closure region.

Dimensionless cavity lengths versus cavitation number for both a blunt cylinder and the case with a spherical head are shown in Fig. 14. For both geometries, the cavity length is increased as the cavitation number is reduced. At a constant cavitation number, a longer cavity length is provided by the blunt cylinder. It can be concluded that the smooth geometry change in a cylinder with a spherical head generates a smaller cavity region. The same argument can be made for cavity diameter for the two shapes as displayed in Fig. 15. The results of the two methods as seen in both Fig. 14 and 15 agree well with each other. The VOF model, however, predicts larger values for the cavity diameter due to the existence of reentrant jet.

4. CONCLUSION

In this paper, the super- and partial- cavitation over axisymmetric bodies is studied using two numerical methods: VOF technique and boundary element method (BEM). The results of the two methods agree well with each other and with those of the experiments for simple cavitators. Two different geometries for a cone with various cone angles were considered. Also, the results of comparison between the two methods for partial cavitation over a sphere, a blunt cylinder, and a cylinder with a spherical head were presented. For cavity simulations over a cylinder, the VOF method can accurately predict the flow behavior even near the closure region. In the BEM method, however, a better model is needed to be implemented for treating this region.

REFERENCES

[1] Mohammad P. Fard and E. Roohi. Transient Simulations of Cavitating Flows using a Modified Volume-of-Fluid (VOF) Technique. *International Journal of CFD (IJCFD)* 22(1,2):97–114, 2008

[2] Abraham N. Varghese, James S. Ohlman and Ivan N. Kirschner. High-speed bodies in partially cavitating axisymmetric flow. *In proceedings of Fifth International Symposium on Cavitation (CAV2003),* Osaka, Japan, Nov 2003

[3] Xiaoxing Peng, Zhi Wang, Sensen Pan and Kai Yan. Generation mechanism of ventilated supercavitation in an axisymmetric body with cavitator. *In proceedings of Sixth International Symposium on Cavitation, CAV2006,* Wageningen, The Netherlands, September 2006

[4] G. Wang, I. Senocak, W. Shyy, T. Ikohagi, and S. Cao. Dynamics of attached turbulent cavitating flows. *Journal of Aerospace Sciences,* 37, pp. 551-581, 2001

[5] W. Yuan, J. Sauer and G.H. Schnerr. Modeling and computation of unsteady cavitation flows in injection nozzles. *J. of Mechanical Ind.* Vol. 2, pp. 383-394, 2001

[6] N. H. Singhal, A.K. Athavale, M. Li, and Y. Jiang. Mathematical basis and validation of the full cavitation model. *J. of Fluids Engineering,* Vol. 124, pp. 1-8, 2002

[7] C.L. Merkle, J. Feng, and P.E.O. Buelow. Computational modeling of the dynamics of sheet cavitation. *In Proceedings of the 3rd International Symposium on Cavitation, (CAV1998),* Grenoble, France, 1998

[8] R.F. Kunz, D. A. Boger, D. R. Stinebring, T.S. Chyczewski, J.W. Lindau, and H. J. Gibeling. A preconditioned Navier-Stokes method for two-phase flows with application to cavitation. *Journal of Computers & Fluids,* Vol. 29, pp. 849-875, 2000

[9] M. Frobenius and R. Schilling. Three-dimensional unsteady cavitating effects on a single hydrofoil and in a radial pump- measurement and numerical simulation. *In Proceedings of the 5th International Symposium on Cavitation (CAV2003)*, Osaka, Japan, Nov 2003

[10] S. Wiesche. Numerical simulation of cavitation effects behind obstacles and in an automotive fuel jet pump. *Journal of Heat Mass Transfer,* Vol. 41, pp. 615-624, 2005

[11] D.L. Youngs. Time dependent multi material flow with large fluid distortion. *Journal of Numerical Methods for Fluid Dynamics,* N.Y, 273-285, 1982

[12] J.L. Hess, A.M.O. Smith. Calculation of potential flow about arbitrary three-dimensional bodies.

Progress in Aeronautical Science, Vol. 8, pp. 1–138, Pergamon Press, New York, 1966

[13] J.S. Uhlman. The Surface Singularity Method Applied to Partially Cavitating Hydrofoils. *Journal of Ship Research*, 31, 2. 1987

[14] J.S. Uhlman. The Surface Singularity or Boundary Integral Method Applied to Supercavitating Hydrofoils. *Journal of Ship Research,* 33, 1. 1989

[15] S. A. Kinnas, and N.E. Fine. Nonlinear Analysis of the Flow Around Partially and Super-Cavitating Hydrofoils by a Potential Based Panel Method. *Proceedings of the IABEM-90 Symposium, International Association for Boundary Element Methods,* Rome, Italy, 1990

[16] S.A. Kinnas, and N.E. Fine. A Numerical Nonlinear Analysis of the Flow Around Two- and Three-Dimensional Partially Cavitating Hydrofoils. *Journal of Fluid Mechanics*, 254. 1993

[17] A.N. Varghese, J.S. Uhlman, and I.N. Kirschner. Axisymmetric Slender-Body Analysis of Supercavitating High-Speed Bodies in Subsonic Flow. *Proceedings of the Third International Symposium on Performance Enhancement for Marine Applications,* T. Gieseke, editor, Newport, RI, 1997

[18] I.N. Kirschner, J.S. Uhlman, Jr., A.N. Varghese, and I.M. Kuria. Supercavitating Projectiles in Axisymmetric Subsonic Liquid Flows. *Proceedings of the ASME & JSME Fluids Engineering Annual Conference & Exhibition, Cavitation and Cavitation and Multiphase Flow Forum, FED 210,* J. Katz and Y. Matsumoto, editors, Hilton Head Island, SC, 1995

[19] J.S. Uhlman, A.N. Varghese, and I.N. Kirschner. Boundary Element Modeling of Axisymmetric Supercavitating Bodies. *Proceedings of the 1st Symposium on Marine Applications of Computational Fluid Dynamics,* Hydrodynamic/Hydroacoustic Technology Center, McLean, VA, 1998

[20] Y.N. Savchenko, V.N. Semenenko, Y.I. Naumova, A.N. Varghese, J.S. Uhlman, and I.N. Kirschner. Hydrodynamic Characteristics of Polygonal Contours in Supercavitating Flow. *Proceedings of the Third International Symposium on Performance Enhancement for Marine Applications* , T. Gieseke, editor, Newport, RI, 1997

[21] Multiphase Flow Forum, FED 210. J. Katz and Y. Matsumoto, editors, *Hilton Head Island, SC.*

[22] F.H. Hirt and B.D. Nichols. A computational method for free surface hydrodynamics. *Journal of Computational Phys.,* Vol. 39, p. 201, 1981

[23] J.U. Brackbill, D.B. Kothe and C. Zamach. A continuum method for modeling surface tension, Comp. Physics. *Journal of Computational Phys.,* Vol. 100, pp. 335-354, 1992

[24] I. Senocak and W. Shyy. Evaluation of cavitation models for Navier-Stokes computations. *Proceeding of FEDSM 02, ASME Fluid Engineering Division Summer Meeting,* Montreal, Canada, 2002

[25] J.P. Franc and J.M. Michel. *Fundamentals of Cavitation. Section: 6. Kluwer Academic Publisher,* Netherlands, 2004.R.E.

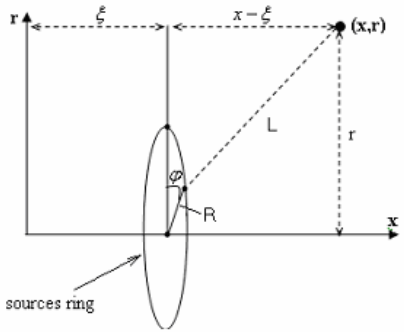

Figure 1. Source ring in a cylindrical coordinate for BEM method.

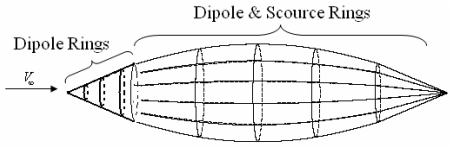

Figure 2. Applying superposition of the free stream, with distributions of the dipoles and sources rings on the interface of the body and the cavity, to solve cavitation in BEM method.

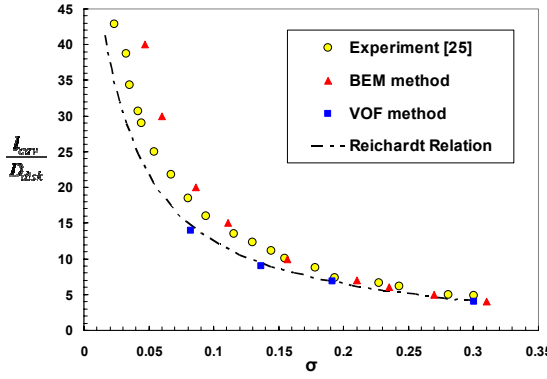

Figure 3. Dimensionless cavity length vs. cavitation number for a disk cavitator from experiments [25], theory, and the two models of VOF and BEM.

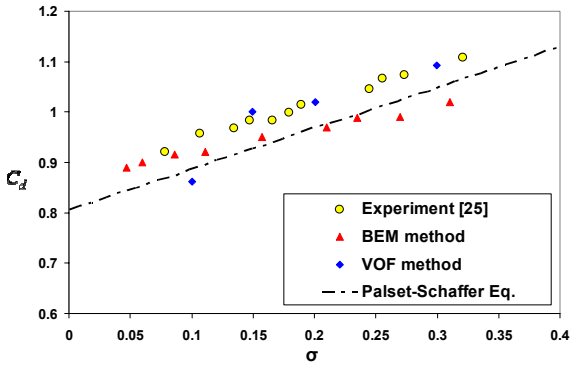

Figure 4. Drag coefficient vs. cavitation number for a disk cavitator from experiments [25], theory, and the two models of VOF and BEM.

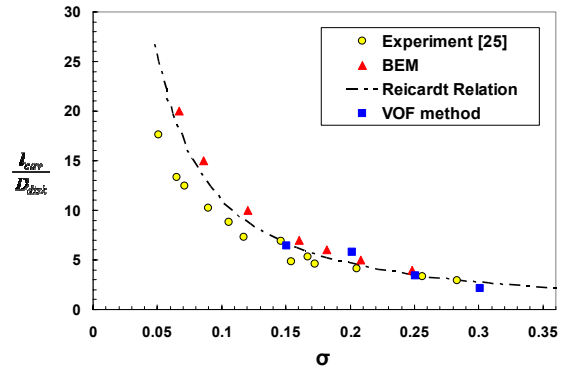

Figure 5. Dimensionless cavity length vs. cavitation number for a cone cavitator with an angle of 90º from experiments [25], theory, and the two models of VOF and BEM.

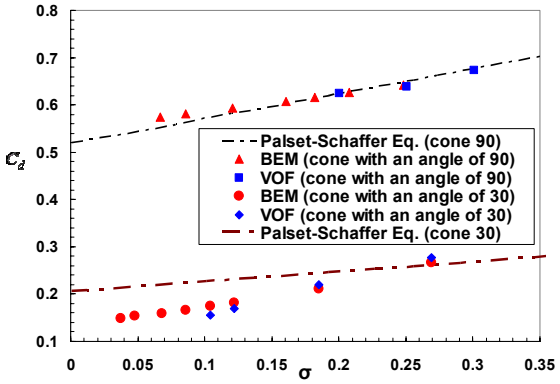

Figure 6. Drag coefficient vs. cavitation number for two cone cavitators with angles of 90º and 30º. The results are shown from theory and the two models of VOF and BEM.

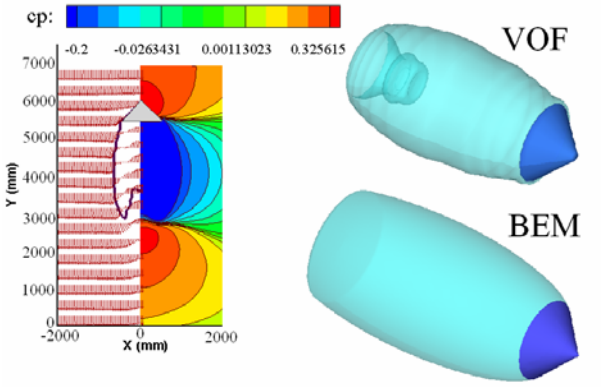

Figure 7. The steady shape of the cavity from the VOF (top) and BEM (bottom) methods for a cone cavitator with an angle of 90º for a cavitation number of σ=0.18. The left image shows the VOF results for the C_p and velocity distribution.

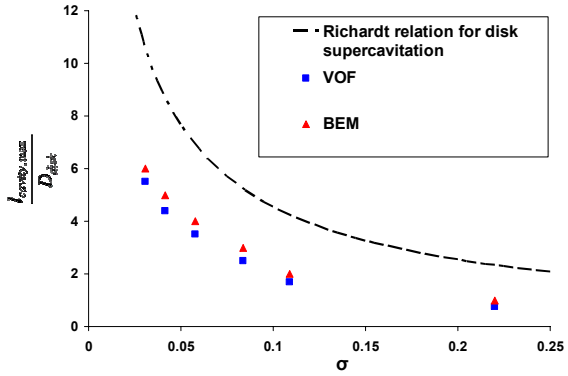

Figure 8. Dimensionless cavity length vs. cavitation number behind a sphere. The theoretical results for a disk cavitator is only displayed to show the difference between the results for a disk and a sphere.

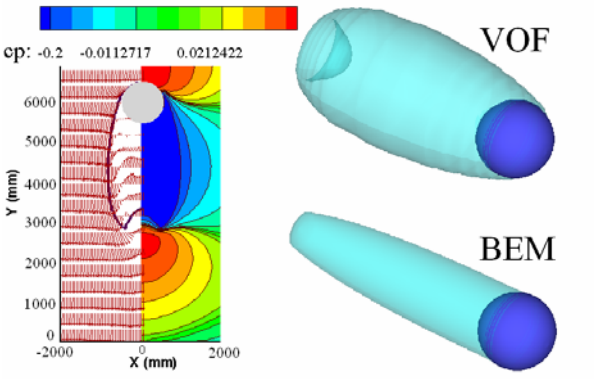

Figure 9. The steady shape of the cavity from the VOF (top) and BEM (bottom) methods for a spherical cavitator for a cavitation number of σ =0.08. The left image shows the VOF results for the C_p and velocity distribution.

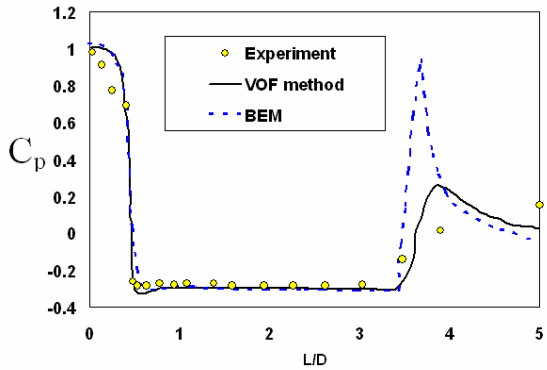

Figure 10. Pressure coefficient vs. nondimensional length for a blunt cylinder for a cavitation number of σ =0.3 from experiments [25] and the two models of VOF and BEM.

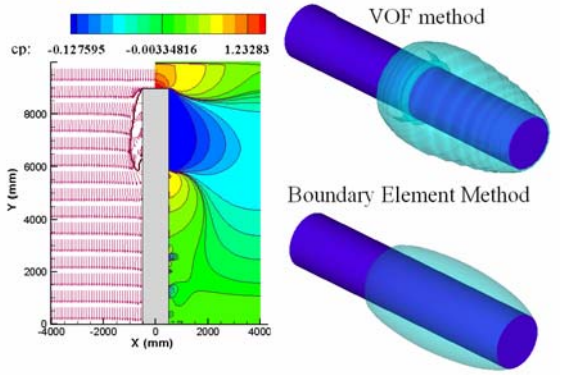

Figure 11. The steady shape of the cavity from the VOF (top) and BEM (bottom) methods for a blunt cylinder for σ =0.3. The left image shows the VOF results for the C_p and velocity distribution.

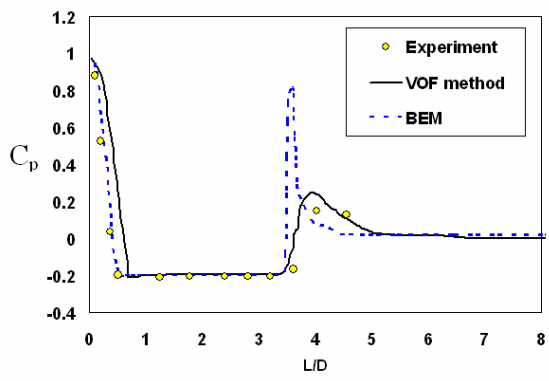

Figure 12. Pressure coefficient vs. nondimensional length for a cylinder with a spherical head for σ =0.2 from experiments [25] and the two models of VOF and BEM.

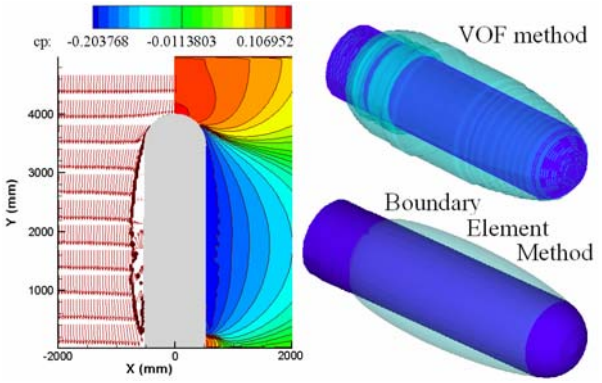

Figure 13. The steady shape of the cavity from the VOF (top) and BEM (bottom) for a cylinder with a spherical head for σ = 0.2. The left image shows the VOF results for the C_p and velocity distributions.

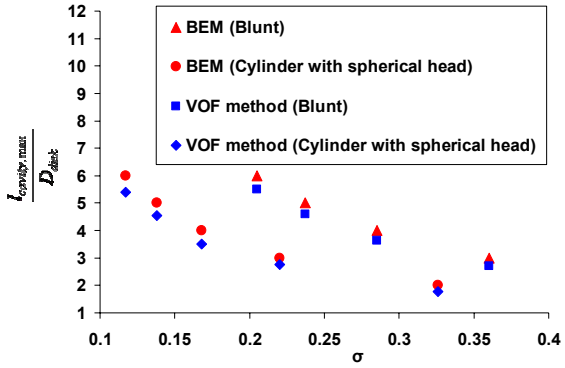

Figure 14. Dimensionless cavity length vs. cavitation number for a blunt cylinder and a cylinder with a spherical head from the two models of VOF and BEM.

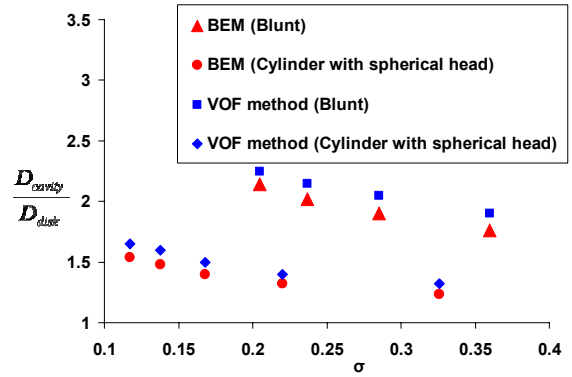

Figure 15. Dimensionless cavity diameter vs. cavitation number a blunt cylinder and a cylinder with a spherical head from the two models of VOF and BEM.